



Microstructure and mechanical properties of nickel-based superalloy fabricated by laser powder-bed fusion using recycled powders

De-cheng Kong, Chao-fang Dong, Xiao-qing Ni, Liang Zhang, Rui-xue Li, Xing He, Cheng Man, and Xiao-gang Li

Cite this article as:

De-cheng Kong, Chao-fang Dong, Xiao-qing Ni, Liang Zhang, Rui-xue Li, Xing He, Cheng Man, and Xiao-gang Li, Microstructure and mechanical properties of nickel-based superalloy fabricated by laser powder-bed fusion using recycled powders, *Int. J. Miner. Metall. Mater.*, 28(2021), No. 2, pp. 266-278. <https://doi.org/10.1007/s12613-020-2147-4>

View the article online at [SpringerLink](#) or [IJMMM Webpage](#).

Articles you may be interested in

Zhi-yuan Zhu, Yuan-fei Cai, You-jun Gong, Guo-ping Shen, Yu-guo Tu, and Guo-fu Zhang, [Isothermal oxidation behavior and mechanism of a nickel-based superalloy at 1000](#), *Int. J. Miner. Metall. Mater.*, 24(2017), No. 7, pp. 776-783. <https://doi.org/10.1007/s12613-017-1461-y>

Adam Khan Mahaboob Basha, Sundarajan Srinivasan, and Natarajan Srinivasan, [Studies on thermally grown oxide as an interface between plasma-sprayed coatings and a nickel-based superalloy substrate](#), *Int. J. Miner. Metall. Mater.*, 24(2017), No. 6, pp. 681-690. <https://doi.org/10.1007/s12613-017-1451-0>

A. I. Noskov, A. Kh. Gilmutdinov, and R. M. Yanbaev, [Effect of coaxial laser cladding parameters on bead formation](#), *Int. J. Miner. Metall. Mater.*, 24(2017), No. 5, pp. 550-556. <https://doi.org/10.1007/s12613-017-1436-z>

Hui-ping Duan, Xiao Liu, Xian-zhe Ran, Jia Li, and Dong Liu, [Mechanical properties and microstructure of 3D-printed high Co-Ni secondary hardening steel fabricated by laser melting deposition](#), *Int. J. Miner. Metall. Mater.*, 24(2017), No. 9, pp. 1027-1033. <https://doi.org/10.1007/s12613-017-1492-4>

George Z. Chen, [Interactions of molten salts with cathode products in the FFC Cambridge Process](#), *Int. J. Miner. Metall. Mater.*, 27(2020), No. 12, pp. 1572-1587. <https://doi.org/10.1007/s12613-020-2202-1>

Erdem Karakulak, [Characterization of Cu-Ti powder metallurgical materials](#), *Int. J. Miner. Metall. Mater.*, 24(2017), No. 1, pp. 83-90. <https://doi.org/10.1007/s12613-017-1381-x>



IJMMM WeChat



QQ author group

Microstructure and mechanical properties of nickel-based superalloy fabricated by laser powder-bed fusion using recycled powders

De-cheng Kong¹⁾, Chao-fang Dong¹⁾, Xiao-qing Ni²⁾, Liang Zhang²⁾, Rui-xue Li¹⁾, Xing He¹⁾, Cheng Man³⁾, and Xiao-gang Li¹⁾

1) Beijing Advanced Innovation Center for Materials Genome Engineering, University of Science and Technology Beijing, Beijing 100083, China

2) Shanghai Engineering Research Center of 3D Printing Materials, Shanghai Research Institute of Materials, Shanghai 200437, China

3) School of Materials Science and Engineering, Ocean University of China, Qingdao 266100, China

(Received: 20 June 2020; revised: 21 July 2020; accepted: 21 July 2020)

Abstract: Evaluating the recyclability of powders in additive manufacturing has been a long-term challenge. In this study, the microstructure and mechanical properties of a nickel-based superalloy fabricated by laser powder-bed fusion (LPBF) using recycled powders were investigated. Re-melted powder surfaces, satellite particles, and deformed powders were found in the recycled powders, combined with a high-oxygen-content surface layer. The increasing oxygen content led to the formation of high-density oxide inclusions; moreover, printing-induced cracks widely occurred and mainly formed along the grain boundaries in the as-built LPBF nickel-based superalloys fabricated using recycled powders. A little change in the Si or Mn content did not increase the hot cracking susceptibility (HCS) of the printed parts. The changing aspect ratio and the surface damage of the recycled powders might contribute to increasing the crack density. Moreover, the configuration of cracks in the as-built parts led to anisotropic mechanical properties, mainly resulting in extremely low ductility vertical to the building direction, and the cracks mainly propagated along the cellular boundary owing to the existence of a brittle precipitation phase.

Keywords: laser powder-bed fusion; recycled powder; cracking; anisotropy; nickel-based superalloy

1. Introduction

Metal additive manufacturing (MAM) has been a popular topic since it was conceived by David Jones in 1974 and developed by Chuck Hull in 1984 as an emerging fabrication technique, which is currently challenging for multiple conventional repetitive manufacturing methods [1]. The main principle of MAM is the layer-by-layer quick-melting of metallic powders or wires using minimal heat, to efficiently fabricate a given material/component with a specific shape and size [2–7]. Studies on MAM fabrication have garnered attention in both scientific research and engineering applications; moreover, MAM fabrication, as with other emerging new processing techniques, has been adequately applied in developing and printing diverse materials [8–10].

To date, laser powder-bed fusion (LPBF) remains the most prevalent additive manufacturing technique for metals and alloys compared with other MAM methods, such as directed energy deposition and material extrusion. Components manufactured via this technique have been reported to fea-

ture excellent dimensional accuracy, low porosity, and minimal cracking issue [11–14]; however, defects, such as unmelted powders [15–16], cracks [17–18], gas pores [19–21], balling [22–24], and rough surfaces [25–26] can still exist in the printed components and significantly influence their service performance. Hence, researchers have sought comprehensive data to optimize the printing parameters for specific materials to minimize these problems [27–31]. Among the multiple printing condition parameters, the powder property is one of the most critical factors. During the selective laser melting process, only a small portion of powders are melted to fabricate the designed parts. The surrounding powders are partially heat-affected, and most of the feedstock powders are left unmelted and can be recycled. However, the crucial issue in powder recycling is to sieve the reusable powders from the recycled powders and ensure that high-quality powders with properties similar to those of the virgin powders are obtained [32–35]. Thus, evaluating powder recyclability in LPBF has been a primary concern for many researchers. At present, many researchers focus on the properties of the re-

cycled nickel-based superalloy powders, such as geometric factors, surface texture, rheological characteristics, and packing behavior. Nguyen *et al.* [36] confirmed that more spherical powders and fewer satellite particles would promote better flowability and packing capability. Deng *et al.* [37] found that moisture-induced oxidation during powder recycling and the incorporation of spatter particles during printing would result in higher oxygen content in the LPBF-produced parts. However, the quality of the parts printed using recycled powders has not been widely investigated, especially in terms of mechanical response.

Nickel-based superalloys have attracted increasing attention in the LPBF field owing to their broad applications, given their excellent creep properties, oxidation resistance, and hot corrosion resistance [38–39]. However, hot cracking, or tearing, is a challenge for the printed nickel-based superalloys with a high thermal expansion coefficient. The printed cracks are the result of residual stresses arising from the rapid solidification of an alloy, and they limit the achievable strength and ductility of the materials [40–42]. Using recycled powders will undoubtedly affect the printability of the nickel-based superalloys, since hot cracking is related to several metallurgical factors, such as composition change, powder property, and solidification temperature range [43–44]. Therefore, the effects of using recycled powders on cracking should also be considered.

To this end, a nickel-based superalloy was fabricated by

LPBF using recycled powders in this work. The microstructures of the reused powders and the bulk LPBF nickel-based superalloys were characterized via electron backscatter diffraction (EBSD) and electron channeling contrast imaging (ECCI). Tensile tests were conducted to investigate the mechanical property of the LPBF nickel-based superalloys, and the results were compared with those of the LPBF nickel-based superalloys fabricated using fresh powders from the literature.

2. Experimental

2.1. Material preparation

The LPBF nickel-based superalloys were produced using the EOS M290 printer; the detailed printing parameters are described in Table 1. The powders were used for six cycles; the average time for each cycle was about 80 h, and the reused powders were sieved at 70 µm. The powder layers were scanned in a continuous laser mode according to a zigzag pattern, alternating by 67° between layers to reduce the stress concentration and texture. To avoid or alleviate the effect of printing-induced residual stress, all samples were heat-treated under 300°C for 1 h and cooled in air. The chemical compositions of the LPBF nickel-based superalloys (Table 2), detected by an electric spark spectrometer, were all in the standard range for traditional counterparts, and the oxygen content was around 350 ppm.

Table 1. Detailed printing parameters of the as-built LPBF nickel-based superalloy

Baseplate temperature / °C	Laser power / W	Scanning rate / (mm·s ⁻¹)	Hatch distance / µm	Powder thickness / µm
80	280	960	110	40

Table 2. Chemical compositions of the LPBF nickel-based superalloy

C	Si	Mn	P	Cr	Mo	Fe	Ni	wt%
0.080	0.39	0.49	0.008	22.12	8.76	19.01	Balance	

2.2. Microstructural characterization

Samples were mechanically ground with a series of SiC papers up to 3000# grit and then polished using diamond suspension with particle size down to 1 µm together with 40 nm colloidal SiO₂ polishing suspension. Finally, the polished samples were ultrasonically cleaned in an acetone bath for 30 min. The EBSD data were recorded under 25 kV high voltage with a working distance of 17.00 mm in a TESCAN MIRA 3 scanning electron microscope, and the scanning step size was 1 µm. The kernel average misorientation (KAM) calculation was based on the first nearest kernel with perimeter only. Moreover, ECCI measurements were conducted with an acceleration voltage of 20 kV and a working distance of 8.00 mm under optimized diffraction conditions.

2.3. Tensile test

A uniaxial tensile experiment was carried out using the Gatan MTEST2000 micromechanical testing system, and the strain evolution was captured using digital image correlation and analyzed via GOM software. The strain rate was set as 2.5×10^{-4} s⁻¹, and the preload force was set as 30 N. A dog bone-shaped sample with a thickness of 1 mm, gauge length of 6.5 mm, and gauge width of 2.5 mm was prepared via electrical discharge machining. Specimens were ground sequentially with emery papers down to 2000# grit, and the tensile directions were applied both vertical and parallel to the building direction.

2.4. Thermo-Calc simulation

The thermodynamic simulation was conducted using Thermo-Calc simulation for the nickel-based superalloys based on the TCNI9: Ni-Alloys v9.1 database. The equilibrium step diagram for the nickel-based superalloy with the composition Ni–22.0Cr–19.0Fe–9.9Mo–0.5Mn–0.4Si–0.03 O (in wt%) was calculated. The Scheil model was used to

evaluate the hot cracking issue, and herein, we mainly considered the fraction of solid as a function of temperature for nickel-based superalloys with various Si and Mn contents.

3. Results and discussion

Figs. 1(a) and 1(b) show the scanning electron microscopy (SEM) images of reused nickel-based superalloy powders at different magnifications, and the arrows indicate re-melted particles, with small satellite particles sintered on them; moreover, some powders featured a dendritic microstructure, due to the heat effect. As a result, the shape of the reused particles was irregular. Fig. 1(c) displays the fraction and cumulative fraction versus the aspect ratio of the reused powders; the figure indicates that there was a significant shape deviation from the spherical nature. Fig. 1(d) shows the cross-sectional morphology of the reused powders, and the related inverse pole figure (IPF) + image quality (IQ) maps and KAM + IQ maps are shown in Figs. 1(e) and 1(f). In the re-melted powder, there was a re-melted layer consisting of tiny grains, due to the fast solidification at the powder surface, and a micro-pore also occurred at the interface between the re-melted layer and raw powder (Fig. 1(e)). The micro-pores in these powders could trap gas and affect the density of the printed parts during melting by releasing the trapped

gas. For the deformed powder (Fig. 1(f)), high residual stress would occur in the deformed region, as seen from the KAM result. Both phenomena above would affect the quality of the printed counterpart.

Fig. 2 shows the total oxygen content evolution of the powders after reusing for different cycles and compares the result with that of previous works [45]. The oxygen content increased with the reuse cycles; it increased quickly at the initial stage and became slow later. For the investigated powders, the oxygen content after reusing for six cycles was about 1.5 times its original content. The micro-scale powders used for LPBF are usually produced by gas or liquid atomization, and a skinny oxide layer can form on the powder surface during these processes [46–47]. This oxide layer on the powder surface can be ruptured and melted, and it releases oxygen on interaction with the high-energy laser. Meanwhile, the gas impurities in the LPBF process atmosphere can be another oxygen source for the printed parts. Owing to the low solubility of oxygen in alloys, oxygen typically exists in the form of oxides during the rapid solidification, and the oxide composition is primarily dependent on the oxygen-gettering elements in the alloys [48–49]. As reported for LPBF 316L stainless steels, Si/Mn-rich oxide inclusions (most below 100 nm) were widely generated and contributed to the high yield strength of the steel by Orowan bypass strengthening and the

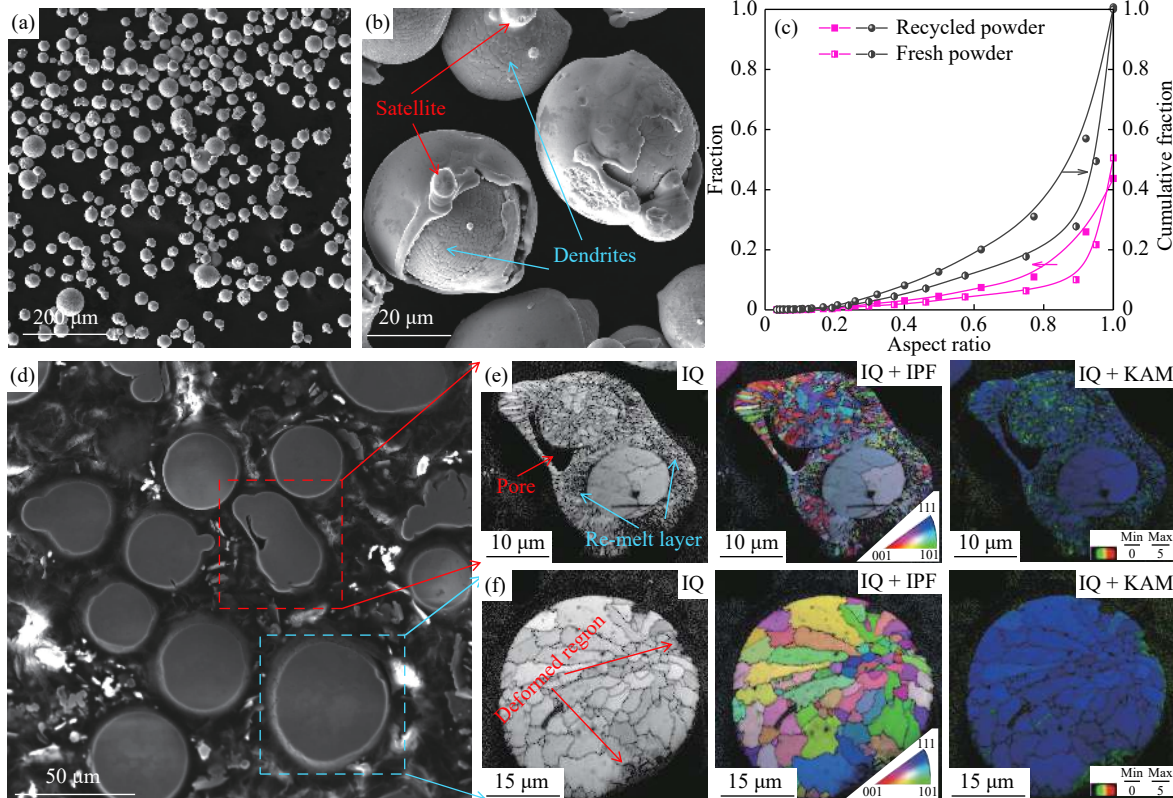


Fig. 1. (a, b) SEM images of reused nickel-based superalloy powders at different magnifications; arrows indicate the re-melted particles with satellite, and dendrites. (c) Fraction and cumulative fraction of the reused powder versus the aspect ratio of the reused powders. (d) Cross-sectional morphology of reused powders. EBSD results for (e) re-melted powder and (f) deformed powder.

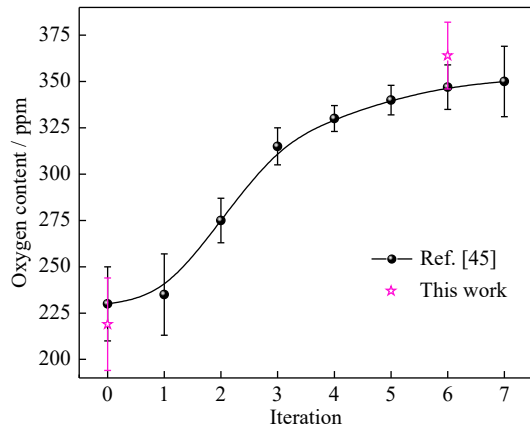


Fig. 2. Oxygen content evolution of the powders after reusing for different cycles and subsequent sieving at 70 μm .

high grain coarsening resistance at high temperatures by Zener pinning [50–51].

Figs. 3(a) and 3(b) show the ECCI results of the as-built LPBF nickel-based superalloy fabricated using recycled powders, considering different planes, with the Z-axis along

the building direction. The white arrows indicate the Mo-enriched precipitates (σ phase), and blue arrows indicate the oxide inclusions according to our previous transmission electron microscopy results [52]. The equilibrium step diagram for the nickel-based superalloy with the composition Ni–22.0Cr–19.0Fe–9.9Mo–0.5Mn–0.4Si–0.03O (wt%) was calculated, as it can provide some insights on the precipitates or inclusions since the rapid melting and solidification were non-equilibrium. The spherical nature and fineness of the oxide inclusions in LPBF components indicate that they were initiated from the melt (Fig. 3(c)). The spinel phase occurred before the start of the matrix solidification (below 1743 K), while the σ phase was generated at a relatively low temperature (below 1400 K). However, owing to the fast solidification, the other phases (i.e., body-centered cubic phase) had no time to form, and this can be confirmed from the following EBSD results. Meanwhile, cellular structures occurred inside the grains (Figs. 3(a) and 3(b)), and the morphologies were different for different planes. The cellular boundary (dislocation cells) was confirmed to be due to the residual stress

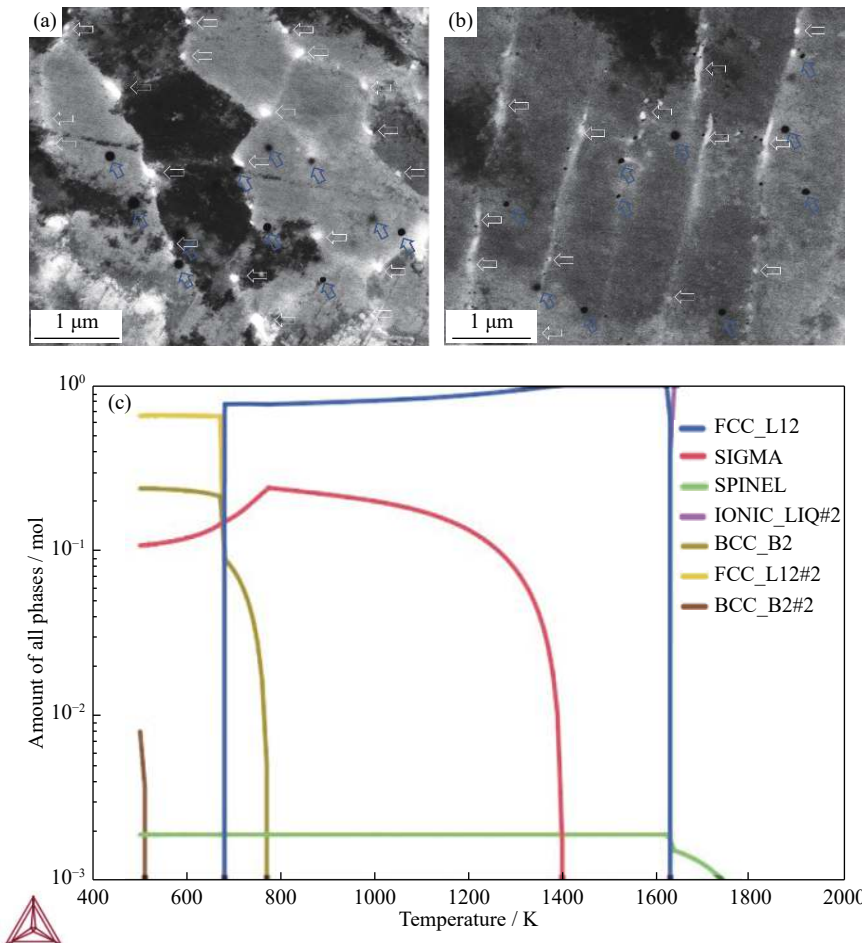


Fig. 3. ECCI results of the as-built LPBF nickel-based superalloy fabricated using recycled powders: (a) XOY plane and (b) XOZ plane; white arrows indicate the Mo-enriched precipitates, and blue arrows indicate oxides. (c) Equilibrium step diagram for the nickel-based superalloy with the composition Ni–22.0Cr–19.0Fe–9.9Mo–0.5Mn–0.4Si–0.03O.

caused by the intrinsic localized heating/cooling heterogeneities upon laser scanning; at elevated temperatures, the high residual stress can cause plastic deformation [53]. This novel metastable cellular structure has been proved to have substantial effects on the mechanical properties of additively manufactured parts; especially, it increases their yield strength without sacrificing much ductility [54–56]. Moreover, the σ phase mainly precipitated at the cellular boundary, as shown by the white arrows in Figs. 3(a) and 3(b), and the oxide inclusions were confirmed to mainly consist of Si and Mn, which indicates that the induction of oxygen could reduce the Mn and Si contents in the matrix [50].

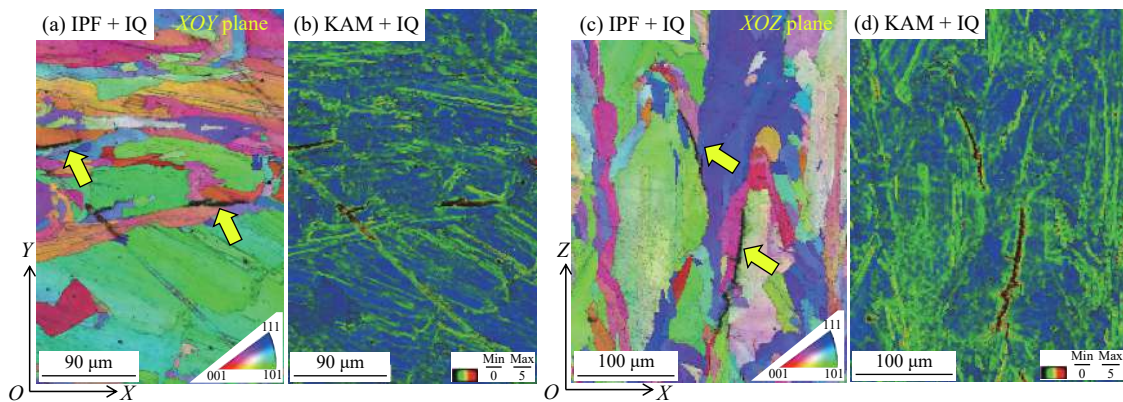


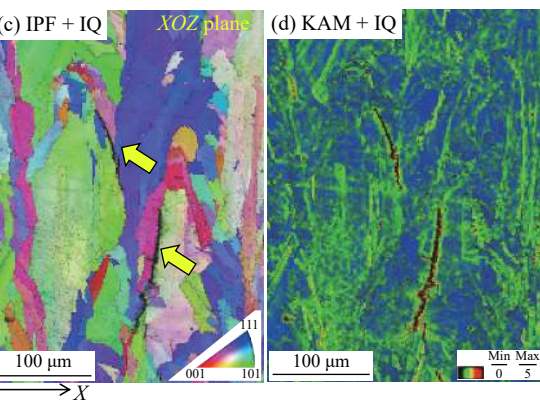
Fig. 4. EBSD results of the as-built LPBF nickel-based superalloy fabricated using recycled powders: (a) IPF + IQ maps and (b) KAM + IQ maps for XOY plane; (c) IPF + IQ maps and (d) KAM + IQ maps for XOZ plane.

Increasing the oxygen content to form the oxide inclusions will reduce the Si and Mn contents in the matrix; therefore, we used Scheil simulation with a thermodynamic database to calculate the effects of the Si and Mn contents on the cracking susceptibility during the fast solidification. Scheil solidification simulation was conducted using the Thermo-Calc software to compute the crack susceptibility coefficient (CSC) and freezing range. The solidification cracking will more easily occur when the solidification temperature range is broad (for a given Gibbs free energy), over which the vulnerable zone is extended; thus, we adopted the hot cracking susceptibility (HCS) parameter in this work. The freezing temperature range is defined as the solidification region of solid mass fraction between 0 and 0.99 and can be expressed as:

$$\Delta T = T_0^S - T_{0.99}^S \quad (1)$$

where ΔT is the temperature difference between a temperature at the solid fraction of 0 (T_0^S) and that at a fraction of 0.99 ($T_{0.99}^S$). Figs. 5(a₁) and 5(b₁) show the temperature as a function of the solid fraction in LPBF nickel-based superalloys for various Si and Mn contents; the solidification temperature range was more sensitive to the Si content, which led to a massive change in the heat release during the solidification, while the heat changed little with the Mn content.

Fig. 4 shows the EBSD results of the as-built LPBF nickel-based superalloy fabricated using recycled powders. The matrix featured the face-centered cubic phase, and some cracks occurred in the matrix. Since the powder layers were scanned in a continuous laser mode, with 67° alternation between layers, the crack direction on the XOY plane should be random, and there was no anisotropic effect for the cracks on the plane. However, the cracks on the XOZ plane were mainly along the building direction (Z-axis), which would cause mechanical anisotropy. Meanwhile, the cracks mainly occurred at the grain boundaries, as shown by the marked arrows in Figs. 4(a) and 4(c).



The CSC parameter can be calculated using the following equation [57]:

$$CSC = \frac{t_V}{t_R} \quad (2)$$

where t_V is the time during solidification in which the matrix is vulnerable to cracking, and t_R is the time available for the stress-relief process. The stress-relief time is defined as the time the solid spends in the fraction range of 0.4 and 0.9 (the range over which liquid feeding can quickly occur). The vulnerable time is defined as the time the solid spends in the fraction range of 0.9 to 0.99. The vulnerable period and the time available for stress-relief processes are expressed as [58]:

$$t_V = t_{0.99} - t_{0.9} \quad (3)$$

$$t_R = t_{0.9} - t_{0.4} \quad (4)$$

where t is the time at the specific mole fraction of solid; that is, $t_{0.99}$ is the time at the mole fraction of a solid of 0.99. Figs. 5(a₂) and 5(b₂) show the mole fraction of solid as a function of time; increasing the Si content could shorten the stress-relief time but increase the vulnerable time, whereas the stress-relief and vulnerable time did not change much with the Mn content. The HCS parameter can be calculated as a product of CSC and the freezing range as follows [59]:

$$HCS = (CSC \times \Delta T)/100 \quad (5)$$

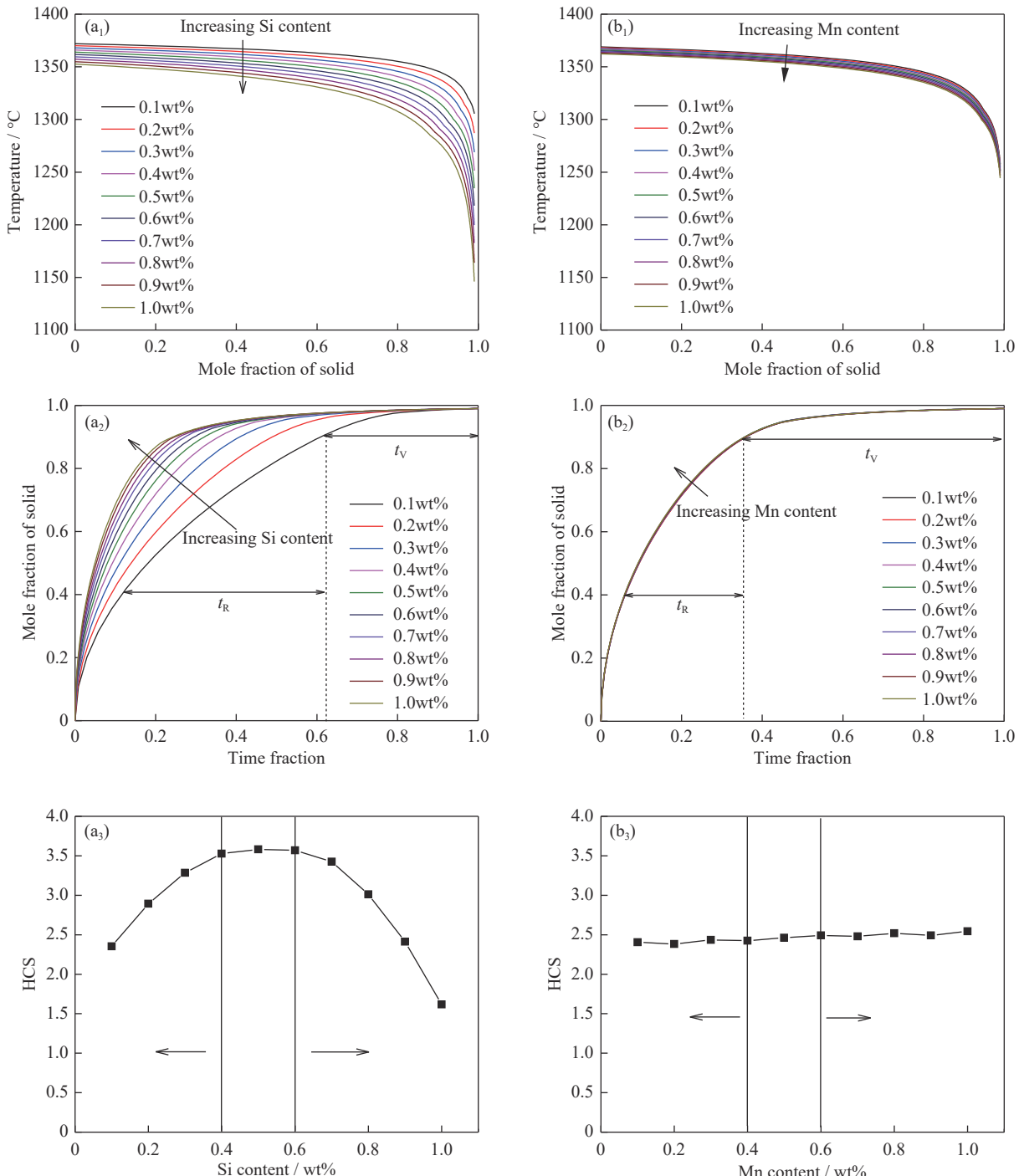


Fig. 5. Temperature as a function of mole fraction of solid in nickel-based superalloy for various contents of (a₁) Si and (b₁) Mn; Mole fraction of solid as a function of time for nickel-based superalloy with various contents of (a₂) Si and (b₂) Mn; HCS value as a function of various contents of (a₃) Si and (b₃) Mn.

Figs. 5(a₃) and 5(b₃) display the HCS values as a function of Si and Mn contents. Interestingly, the Si content in the standard content of the GH3536 superalloy exhibited the largest HCS, and a slight decrease in the Si content or increase in the Si content could reduce the cracking sensitivity. Moreover, the HCS parameter had little relationship with the

Mn content in our test content range. Although the non-equilibrium model cannot reflect the exact cooling speeds in the LPBF process, it is probably the closest modeling method we can use. Thus, the change in the chemical compositions (mainly Si and Mn contents) in our nickel-based superalloys did not worsen the cracking issue.

To investigate the anisotropic mechanical properties of the LPBF nickel-based superalloy, tensile experiments were conducted on different planes, and at least three samples were tested for reproducibility; the results are depicted in Figs. 6(a) and 6(b). Fig. 6(c) shows the yield strength and total elongation results on different planes and compares them with the counterpart fabricated using fresh powders [60]. Both the strength and ductility decreased for the as-built LPBF nickel-based superalloy fabricated using recycled powders, indicating that using recycled powders led to a decrease in the qual-

ity of the printed parts; this should be related to increasing crack densities. However, the change in the composition did not have much effect. This may be due to the decreasing flowability and packing capability of the recycled powders caused by the changing aspect ratio and the surface damage. The decreasing powder flowability would lead to insufficient interaction between the laser heat sources and the powders during melting, which might result in a high density of pores or cracks in the components. Detailed related investigations will be conducted in our future work.

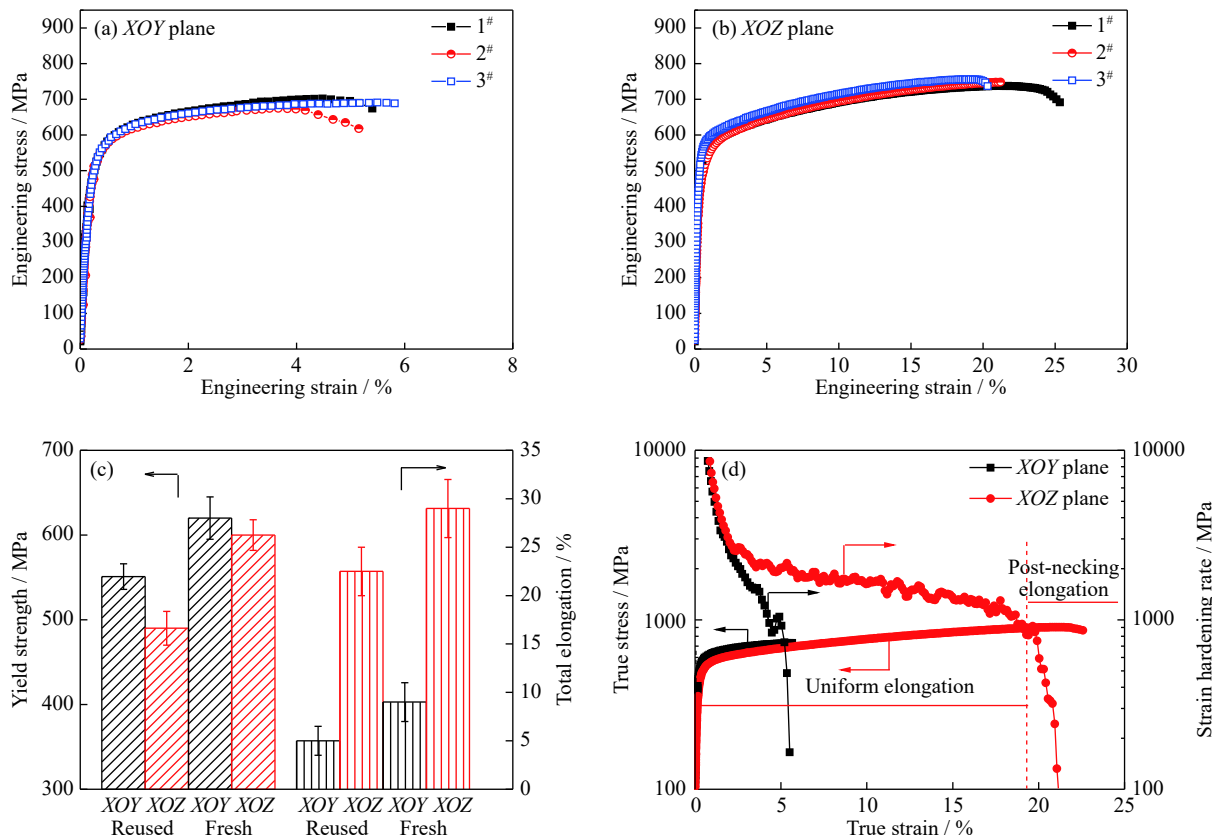


Fig. 6. Engineering strain and stress curves for the as-built LPBF nickel-based superalloy fabricated using recycled powders: (a) XOY plane and (b) XOZ plane, the tensile test was repeated three times. (c) The yield strength and total elongation and (d) the true stress and strain hardening rate curves, respectively.

The yield strength of the printed parts was approximately 500 MPa, much higher than that of the wrought counterpart (380 MPa), which is mainly ascribed to the high-density cellular structures resisting the motion of dislocations [61]. However, the yield strength on the XOY plane was higher than that on the XOZ plane, which should be due to the different spacings of the cellular boundaries along the tensile axis (Figs. 3(a) and 3(b)). The effective distance between the cellular boundary in the XOY plane was smaller than that in the XOZ plane, which provided a stronger resistance via the Hall-Petch effect. Thus, the XOY plane featured a higher strain hardening rate than the XOZ plane (Fig. 6(d)).

Meanwhile, there was a noticeable ductility difference between the XOY plane (~5%) and the XOZ plane (~25%), which should be due to the angle between the tensile direction and the crack direction. Figs. 7 and 8 display the EBSD results of the as-built LPBF nickel-based superalloy fabricated using recycled powders under different strains, considering different planes. On the XOY plane, the loading direction was vertical to the cracking direction, as shown in Fig. 7(a); the stress would quickly accumulate at the crack tip and accelerate the crack propagation. Figs. 7(b₂)–7(d₂) show that the KAM value at the crack tips was much higher than those at the other regions. However, the tensile direction on the

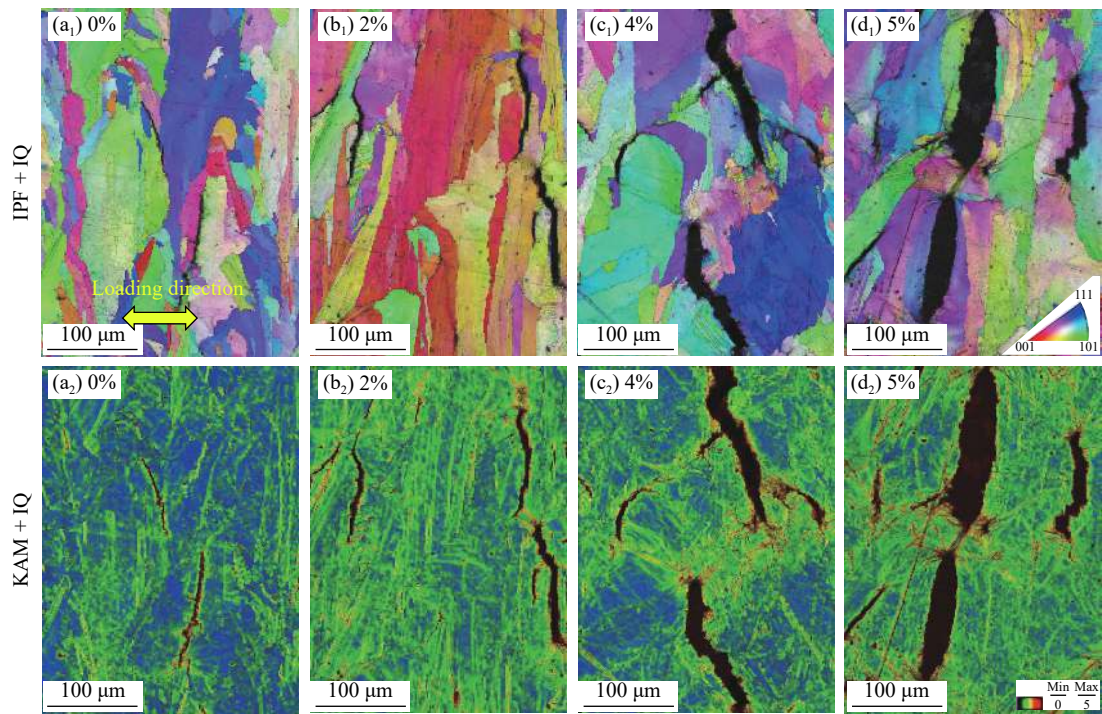


Fig. 7. IPF + IQ maps and KAM + IQ maps of the as-built LPBF nickel-based superalloy fabricated using recycled powders under different strains on XOX plane: (a₁, a₂) no deformation; (b₁, b₂) 2%; (c₁, c₂) 4%; (d₁, d₂) 5%.

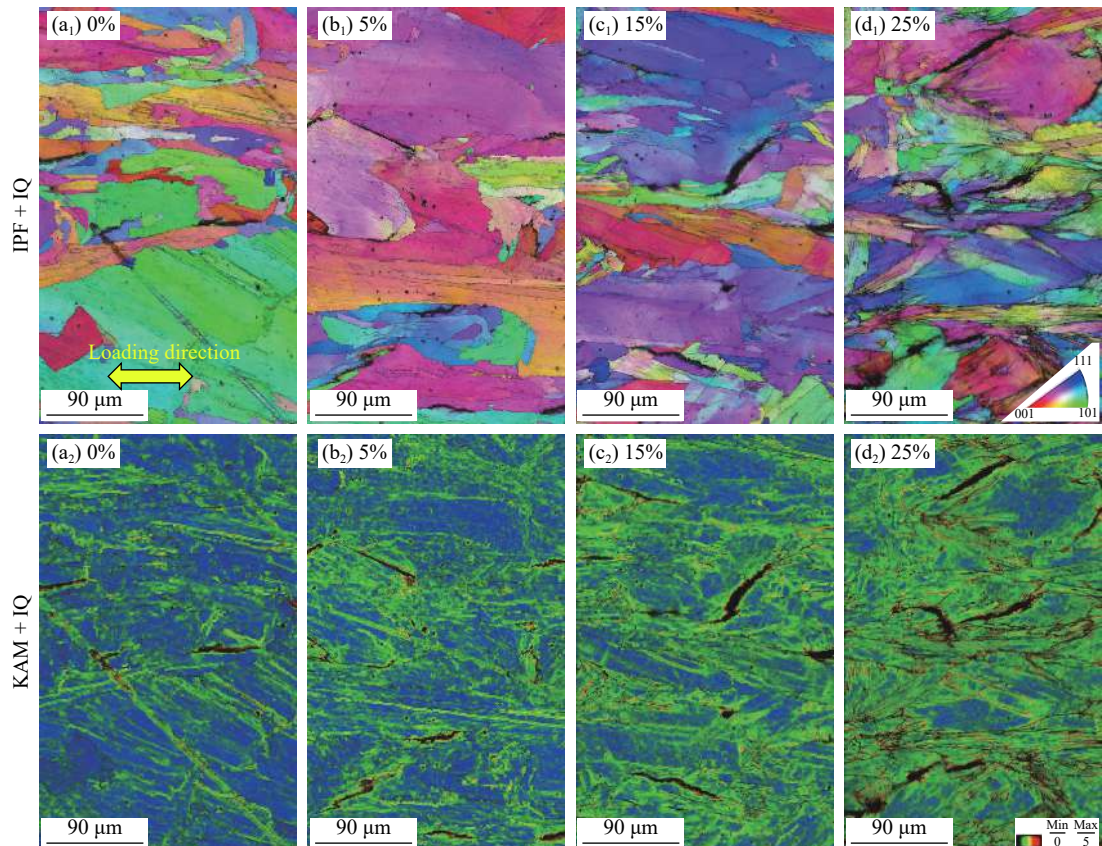


Fig. 8. IPF + IQ maps and KAM + IQ maps of the as-built LPBF nickel-based superalloy fabricated using recycled powders under different strains on XOX plane: (a₁, a₂) no deformation; (b₁, b₂) 5%; (c₁, c₂) 15%; (d₁, d₂) 25%.

XOZ plane was parallel to the crack direction, which provided relatively high resistance to the cracking propagation; therefore, a better ductility was obtained along the building direction compared with that on the XOY plane [62].

Figs. 9(a) and 9(b) show the engineering strain distribution versus the gauge distance before failure and the strain map at different global strains on the two planes. The stress concentrated early with strain on the XOY plane, and once it was formed, rupture immediately occurred. For the XOZ plane, the stress was not concentrated at only one region, which indicates a higher resistance to cracking propagation. Fig. 9(c) displays the crack area fraction evolution with the global strain; the cracking propagation rate on the XOY plane was much faster than that on the XOZ plane.

Fig. 10 shows the fracture on different planes of the as-built LPBF nickel-based superalloy fabricated using re-

cycled powders; the fracture shows the presence of many cracks. For the XOY plane (Fig. 10(b)), the fracture edge did not show a notable sign of plastic deformation, which indicates that the fracture was initiated quickly from the printed cracks. For the XOZ plane, the plastic deformation existed at the fracture edge, and we can see the printed cracks were vertical to the fracture marked as yellow arrows in Fig. 10(d).

Figs. 11 shows the ECCI results of the micro-cracks in the as-built LPBF nickel-based superalloy after deformation for different planes. The yellow arrows in Figs. 11(b) and 11(d) indicate the cracks propagated along the cellular boundary. As a hard and brittle phase, these precipitates have a significantly different deformation ratio from the matrix, which would accelerate the crack initiation and propagation processes [63–64].

In summary, after six cycles, the qualities of the as-built

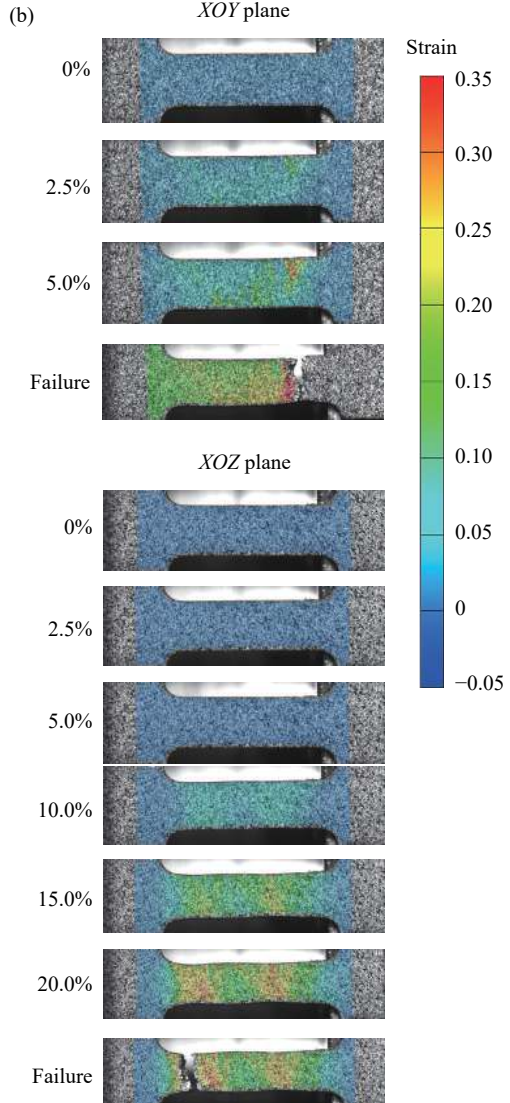
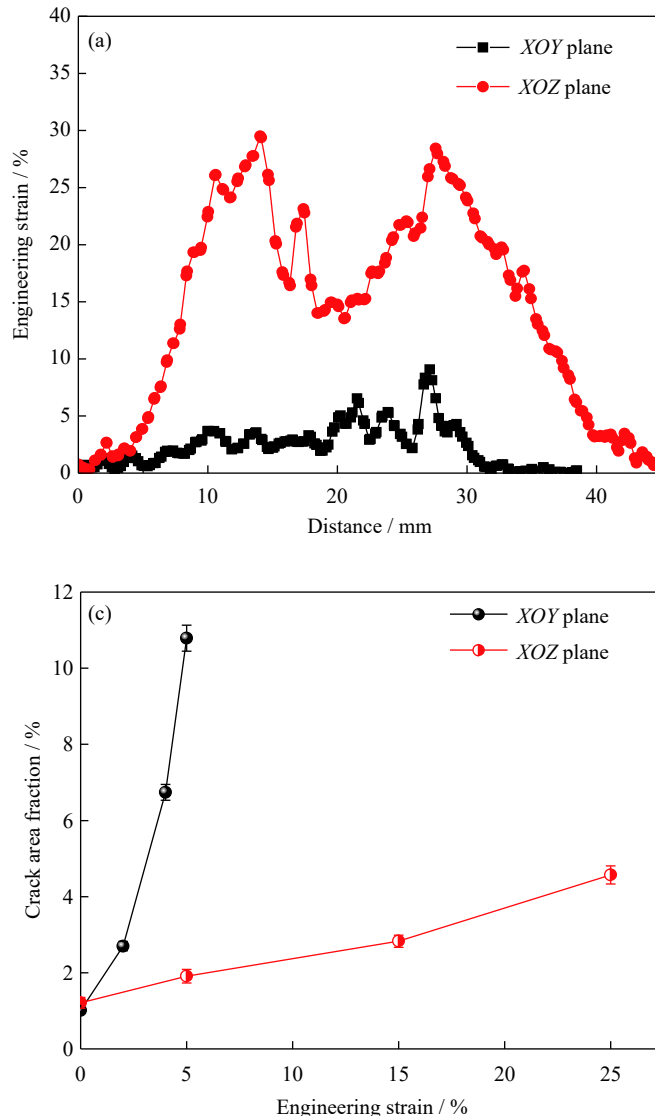


Fig. 9. (a) Engineering strain distribution versus the gauge distance before failure; (b) strain map at different global strains for the two planes; (c) crack area fraction evolution with the engineering strain.

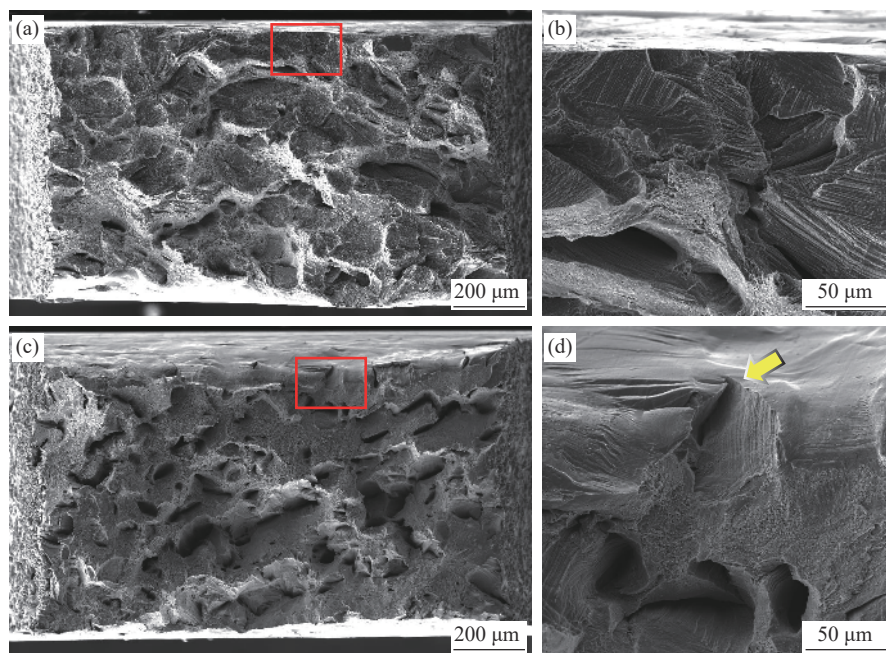


Fig. 10. Fracture of the as-built LPBF nickel-based superalloy fabricated using recycled powders at different magnifications: (a, b) XOY plane; (c, d) XOZ plane.

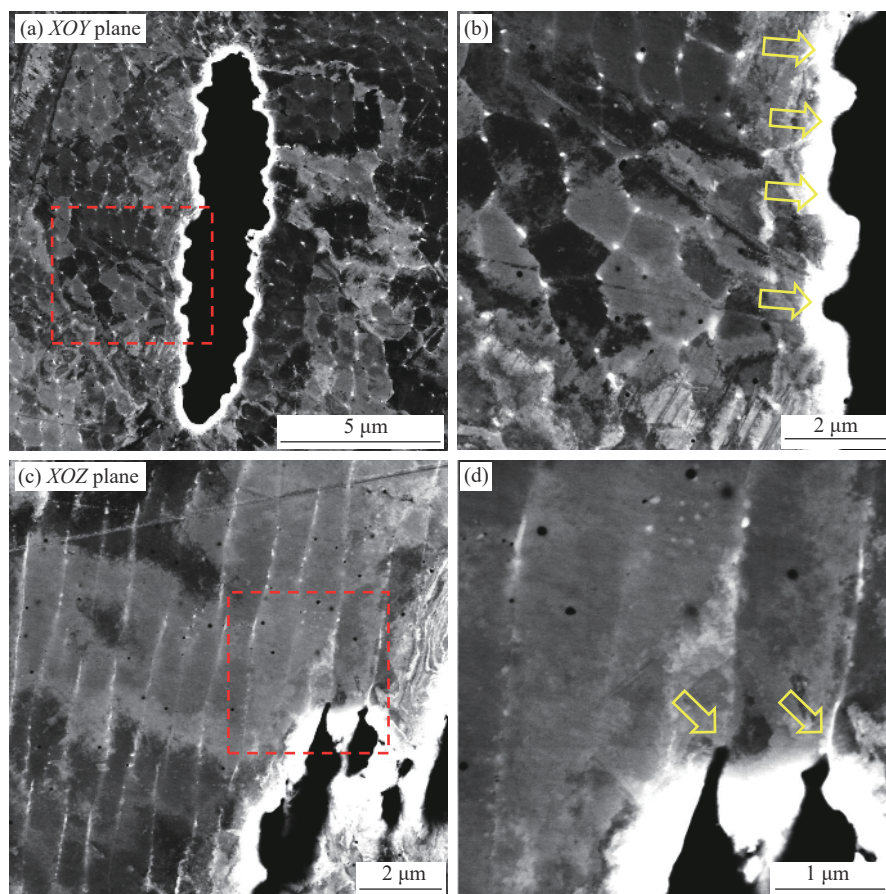


Fig. 11. ECCI results of the as-built LPBF nickel-based superalloy fabricated using recycled powders: (a, b) XOY plane, and the yellow arrows in (b) indicate cracks along the cellular boundary; (c, d) XOZ plane, and the yellow arrows in (d) indicate cracks propagated along the cellular boundary.

LPBF nickel-based superalloy fabricated using recycled powders were not as good as those fabricated using the raw powders, and the mechanical properties degraded accordingly. Therefore, sieving the powder size cannot alone guarantee a high printing quality; more critical requirements need to be considered, such as the powder aspect ratio and oxygen content. Meanwhile, appropriate heat treatment methods, such as hot isostatic pressing, can be adopted to remove these printed defects (i.e., pores and cracks); this way, the powder utilization can be improved.

4. Conclusions

In this work, a nickel-based superalloy was fabricated by LPBF using recycled powders, and the related microstructures were characterized using ECCI and EBSD. The mechanical properties of the as-built LPBF nickel-based superalloys were investigated by tensile tests and compared with those of the counterparts fabricated using fresh powders. The results can provide a basic understanding of the effect of the recycled powder on the quality of the printed nickel-based superalloys and improve the powder utilization in the future. The main conclusions are drawn as follows.

(1) Re-melted powder surfaces, satellite powders, and deformed powders were found in the recycled powder, combined with a high-oxygen-content surface layer; the high oxygen content led to high-density oxide inclusions in the printed parts.

(2) A little change in the Si or Mn content did not increase the HCS of the nickel-based superalloys, and the change in the apparent density of the powders caused by the changing aspect ratio and the surface damage might contribute to increasing the density of printed cracks.

(3) The cracks mainly formed along the grain boundary and the configuration of cracks in the as-built parts led to anisotropic mechanical properties, mainly resulting in extremely low ductility vertical to the building direction.

(4) During the plastic deformation, cracks propagated mainly along the cellular boundaries owing to the prevalent existence of a hard and brittle phase at the boundaries.

Acknowledgements

This work was financially supported by the National Key Research and Development Program of China (No. 2017YFB 0702300), the National Natural Science Foundation of China (No. 51871028), and the Fundamental Research Funds for the Central Universities (No. FRF-TP-19-003B2).

References

- [1] E. MacDonald, and R. Wicker, Multiprocess 3D printing for increasing component functionality, *Science*, 353(2016), No. 6307, art. No. aaf2093.
- [2] M.A. Skylar-Scott, J. Mueller, C.W. Visser, and J.A. Lewis, Voxelated soft matter via multimaterial multinozzle 3D printing, *Nature*, 575(2019), No. 7782, p. 330.
- [3] D.Y. Zhang, S.J. Sun, D. Qiu, M.A. Gibson, M.S. Dargusch, M. Brandt, M. Qian, and M. Easton, Metal Alloys for Fusion-Based Additive Manufacturing, *Adv. Eng. Mater.*, 20(2018), No. 5, p. 1700952.
- [4] A.I. Noskov, A.K. Gilmutdinov, and R.M. Yanbaev, Effect of coaxial laser cladding parameters on bead formation, *Int. J. Miner. Metall. Mater.*, 24(2017), No. 5, p. 550.
- [5] D.C. Kong, C.F. Dong, X.Q. Ni, L. Zhang, C. Man, G.L. Zhu, J.Z. Yao, L. Wang, X.Q. Cheng, and X.Q. Li, Effect of TiC content on the mechanical and corrosion properties of Inconel 718 alloy fabricated by a high-throughput dual-feed laser metal deposition system, *J. Alloys Compd.*, 803(2019), p. 637.
- [6] D.C. Kong, C.F. Dong, X.Q. Ni, L. Zhang, C. Man, J.Z. Yao, Y.C. Ji, Y.P. Ying, K. Xiao, X.Q. Cheng, and X.Q. Li, High-throughput fabrication of nickel-based alloys with different Nb contents via a dual-feed additive manufacturing system: Effect of Nb content on microstructural and mechanical properties, *J. Alloys Compd.*, 785(2019), p. 826.
- [7] D.C. Kong, C.F. Dong, X.Q. Ni, L. Zhang, H. Luo, R.X. Li, L. Wang, C. Man, and X.G. Li, Superior resistance to hydrogen damage for selective laser melted 316L stainless steel in a proton exchange membrane fuel cell environment, *Corros. Sci.*, 166(2020), art. No. 108425.
- [8] D.L. Bourell, Perspectives on Additive Manufacturing, *Ann. Rev. Mater. Res.*, 46(2016), No. 1, p. 1.
- [9] L.E. Murr, E. Martinez, K.N. Amato, S.M. Gaytan, J. Hernandez, D.A. Ramirez, P.W. Shindo, F. Medina, and R.B. Wicker, Fabrication of metal and alloy components by additive manufacturing: examples of 3D materials science, *J. Mater. Res. Technol.*, 1(2012), No. 1, p. 42.
- [10] D.C. Kong, C.F. Dong, X.Q. Ni, L. Zhang, H. Luo, R.X. Li, L. Wang, C. Man, and X.G. Li, The passivity of selective laser melted 316L stainless steel, *Appl. Surf. Sci.*, 504(2020), art. No. 144495.
- [11] S. Van Bael, Y.C. Chai, S. Truscello, M. Moesen, G. Kerckhofs, H. Van Oosterwyck, J.P. Kruth, and J. Schrooten, The effect of pore geometry on the in vitro biological behavior of human periosteum-derived cells seeded on selective laser-melted Ti6Al4V bone scaffolds, *Acta Biomater.*, 8(2012), No. 7, p. 2824.
- [12] C. Haase, J. Bultmann, J. Hof, S. Ziegler, S. Bremen, C. Hinke, A. Schwedt, U. Prahl, and W. Bleck, Exploiting process-related advantages of selective laser melting for the production of high-manganese steel, *Materials*, 10(2017), No. 1, art. No. 56.
- [13] S. Pauly, L. Löber, R. Petters, M. Stoica, S. Scudino, U. Kühn, and J. Eckert, Processing metallic glasses by selective laser melting, *Mater. Today*, 16(2013), No. 1-2, p. 37.
- [14] I. Yadroitsev, L. Thivillon, P. Bertrand, and I. Smurov, Strategy of manufacturing components with designed internal structure by selective laser melting of metallic powder, *Appl. Surf. Sci.*, 254(2007), No. 4, p. 980.
- [15] D.C. Kong, X.Q. Ni, C.F. Dong, X.W. Lei, L. Zhang, C. Man, J.Z. Yao, X.Q. Cheng, and X.G. Li, Bio-functional and anti-corrosive 3D printing 316L stainless steel fabricated by selective laser melting, *Mater. Des.*, 152(2018), p. 88.
- [16] X.Q. Ni, D.C. Kong, Y. Wen, L. Zhang, W.H. Wu, B.B. He, L. Lu, and D.X. Zhu, Anisotropy in mechanical properties and corrosion resistance of 316L stainless steel fabricated by selective

- laser melting, *Int. J. Miner. Metall. Mater.*, 26(2019), No. 3, p. 319.
- [17] J.H. Martin, B.D. Yahata, J.M. Hundley, J.A. Mayer, T.A. Schaedler, and T.M. Pollock, 3D printing of high-strength aluminium alloys, *Nature*, 549(2017), No. 7672, p. 365.
- [18] Z.P. Zhou, L. Huang, Y.J. Shang, Y.P. Li, L. Jiang, and Q. Lei, Causes analysis on cracks in nickel-based single crystal superalloy fabricated by laser powder deposition additive manufacturing, *Mater. Des.*, 160(2018), p. 1238.
- [19] C. Man, C.F. Dong, T.T. Liu, D.C. Kong, D.K. Wang, and X.Q. Li, The enhancement of microstructure on the passive and pitting behaviors of selective laser melting 316L SS in simulated body fluid, *Appl. Surf. Sci.*, 467-468(2019), p. 193.
- [20] A.L. Maximenko and E.A. Oleksy, Pore filling during selective laser melting - assisted additive manufacturing of composites, *Scripta Mater.*, 149(2018), p. 75.
- [21] R. Laquai, B.R. Müller, G. Kasperovich, J. Haubrich, G. Requena, and G. Bruno, X-ray refraction distinguishes unprocessed powder from empty pores in selective laser melting Ti-6Al-4V, *Mater. Res. Lett.*, 6(2018), No. 2, p. 130.
- [22] R.D. Li, J.H. Liu, Y.S. Shi, L. Wang, and W. Jiang, Balling behavior of stainless steel and nickel powder during selective laser melting process, *Int. J. Adv. Manuf. Technol.*, 59(2012), p. 1025.
- [23] D.D. Gu, and Y.F. Shen, Balling phenomena in direct laser sintering of stainless steel powder: Metallurgical mechanisms and control methods, *Mater. Des.*, 30(2009), No. 8, p. 2903.
- [24] X. Zhou, X.H. Liu, D.D. Zhang, Z.J. Shen, and W. Liu, Balling phenomena in selective laser melted tungsten, *J. Mater. Process Technol.*, 222(2015), p. 33.
- [25] T. Sanviemvongsak, D. Monceau, and B. Macquaire, High temperature oxidation of IN 718 manufactured by laser beam melting and electron beam melting: Effect of surface topography, *Corros. Sci.*, 141(2018), p. 127.
- [26] D.C. Kong, C.F. Dong, X.Q. Ni, and X.Q. Li, Corrosion of metallic materials fabricated by selective laser melting, *npj Mater. Degrad.*, 3(2019), No. 1, p. 1.
- [27] X.Q. Ni, D.C. Kong, W.H. Wu, L. Zhang, C.F. Dong, B.B. He, L. Lu, K.Q. Wu, and D.X. Zhu, Corrosion behavior of 316L stainless steel fabricated by selective laser melting under different scanning speeds, *J. Mater. Eng. Perform.*, 27(2018), No. 7, p. 3667.
- [28] D.C. Kong, X.Q. Ni, C.F. Dong, L. Zhang, C. Man, J.Z. Yao, K. Xiao, and X.G. Li, Heat treatment effect on the microstructure and corrosion behavior of 316L stainless steel fabricated by selective laser melting for proton exchange membrane fuel cells, *Electrochim. Acta*, 276(2018), p. 293.
- [29] D.C. Kong, C.F. Dong, X.Q. Ni, L. Zhang, J.Z. Yao, C. Man, X.Q. Cheng, K. Xiao, and X.Q. Li, Mechanical properties and corrosion behavior of selective laser melted 316L stainless steel after different heat treatment processes, *J. Mater. Sci. Technol.*, 35(2019), No. 7, p. 1499.
- [30] S. Gorsse, C. Hutchinson, M. Gouné, R. Banerjee, Additive manufacturing of metals: A brief review of the characteristic microstructures and properties of steels, Ti-6Al-4V and high-entropy alloys, *Sci. Technol. Adv. Mater.*, 18(2017), No. 1, p. 584.
- [31] C.Y. Yap, C.K. Chua, Z.L. Dong, Z.H. Liu, D.Q. Zhang, L.E. Loh, and S.L. Sing, Review of selective laser melting: Materials and applications, *Appl. Phys. Rev.*, 2(2015), No. 4, art. No. 041101.
- [32] A.K.M. Basha, S.Srinivasan, and N. Srinivasan, Studies on thermally grown oxide as an interface between plasma-sprayed coatings and a nickel-based superalloy substrate, *Int. J. Miner. Metall. Mater.*, 24(2017), No. 6, p. 681.
- [33] Y. Sun, M. Aindow, and R.J. Hebert, The effect of recycling on the oxygen distribution in Ti-6Al-4V powder for additive manufacturing, *Mater. High Temp.*, 35(2018), No. 1-3, p. 217.
- [34] A. Hadadzadeh, C. Baxter, B.S. Amirkhiz, and M. Mohammadi, Strengthening mechanisms in direct metal laser sintered AlSi10Mg: Comparison between virgin and recycled powders, *Addit. Manuf.*, 23(2018), p. 108.
- [35] H.P. Tang, M. Qian, N. Liu, X.Z. Zhang, G.Y. Yang, and J. Wang, Effect of powder reuse times on additive manufacturing of Ti-6Al-4V by selective electron beam melting, *JOM*, 67(2015), No. 3, p. 555.
- [36] Q.B. Nguyen, M.L.S. Nai, Z.G. Zhu, C.N. Sun, J. Wei, and W. Zhou, Characteristics of inconel powders for powder-bed additive manufacturing, *Engineering*, 3(2017), No. 5, p. 695.
- [37] P. Deng, M. Karadge, R.B. Rebak, V.K. Gupta, B.C. Prorok, and X.Y. Lou, The origin and formation of oxygen inclusions in austenitic stainless steels manufactured by laser powder bed fusion, *Addit. Manuf.*, 35(2020), art. No. 101334.
- [38] B.K. Narayanan, M. Duraiselvam, S. Natarajan, and M. Anaz Khan, Laser material processing of nickel superalloy for improved erosion resistance, *Mater. Manuf. Process*, 32(2017), No. 14, p. 1596.
- [39] Y.F. Feng, X.M. Zhou, J.W. Zou, and G.F. Tian, Effect of cooling rate during quenching on the microstructure and creep property of nickel-based superalloy FGH96, *Int. J. Miner. Metall. Mater.*, 26(2019), No. 4, p. 493.
- [40] C.L. Qiu, H.X. Chen, Q. Liu, S. Yue, and H.M. Wang, On the solidification behaviour and cracking origin of a nickel-based superalloy during selective laser melting, *Mater. Charact.*, 148(2019), p. 330.
- [41] F. Zhang, L.E. Levine, A.J. Allen, M.R. Stoudt, G. Lindwall, E.A. Lass, M.E. Williams, Y. Idell, and C.E. Campbell, Effect of heat treatment on the microstructural evolution of a nickel-based superalloy additive-manufactured by laser powder bed fusion, *Acta Mater.*, 152(2018), p. 200.
- [42] N.J. Harrison, I. Todd, and K. Mumtaz, Reduction of micro-cracking in nickel superalloys processed by Selective Laser Melting: A fundamental alloy design approach, *Acta Mater.*, 94(2015), p. 59.
- [43] Y. Chen, F.G. Lu, K. Zhang, P.L. Nie, S.R. Elmi Hosseini, K. Feng, and Z.G. Li, Dendritic microstructure and hot cracking of laser additive manufactured Inconel 718 under improved base cooling, *J. Alloys Compd.*, 670(2016), p. 312.
- [44] Q.Q. Han, Y.C. Gu, R. Setchi, F. Lacan, R. Johnston, S.L. Evans, and S.F. Yang, Additive manufacturing of high-strength crack-free Ni-based Hastelloy X superalloy, *Addit. Manuf.*, 30(2019), art. No. 100919.
- [45] A.T. Sutton, C.S. Kriewall, S. Karnati, M.C. Leu, and J.W. Newkirk, Characterization of AISI 304L stainless steel powder recycled in the laser powder-bed fusion process, *Addit. Manuf.*, 32(2020), art. No. 100981.
- [46] J.A. Slotwinski, E.J. Garboczi, P.E. Stutzman, C.F. Ferraris, S.S. Watson, and M.A. Peltz, Characterization of metal powders used for additive manufacturing, *J. Res. Natl. Inst. Stand. Technol.*, 119(2014), p. 460.
- [47] Y. Sun, R.J. Hebert, and M. Aindow, Non-metallic inclusions in 17-4PH stainless steel parts produced by selective laser melting, *Mater. Des.*, 140(2018), p. 153.
- [48] L.E. Murr, S.M. Gaytan, D.A. Ramirez, E. Martinez, J. Hernandez, K.N. Amato, P.W. Shindo, F.R. Medina, and R.B. Wicker, Metal fabrication by additive manufacturing using laser and

- electron beam melting technologies, *J. Mater. Sci. Technol.*, 28(2012), No. 1, p. 1.
- [49] Y.M. Wang, T. Voisin, J.T. McKeown, J.C. Ye, N.P. Calta, Z. Li, Z. Zeng, Y. Zhang, W. Chen, T.T. Roehling, R.T. Ott, M.K. Santala, P.J. Depond, M.J. Matthews, A.V. Hamza, and T. Zhu, Additively manufactured hierarchical stainless steels with high strength and ductility, *Nat. Mater.*, 17(2017), No. 1, p. 63.
- [50] F.Y. Yan, W. Xiong, E. Faierson, and G.B. Olson, Characterization of nano-scale oxides in austenitic stainless steel processed by powder bed fusion, *Scripta Mater.*, 155(2018), p. 104.
- [51] T.R. Smith, J.D. Sugar, C. San Marchi, and J.M. Schoenung, Strengthening mechanisms in directed energy deposited austenitic stainless steel, *Acta Mater.*, 164(2019), p. 728.
- [52] D.C. Kong, X.Q. Ni, C.F. Dong, L. Zhang, C. Man, J.Z. Yao, L. Wang, K. Xiao, and X.G. Li, Anisotropic response in mechanical and corrosion properties of hastelloy X fabricated by selective laser melting, *Constr. Build. Mater.*, 221(2019), p. 720.
- [53] G. Wang, H. Ouyang, Q. Guo, Z.Q. Li, W.T. Yan, Z. Li, and C. Fan, The origin of high-density dislocations in additively manufactured metals, *Mater. Res. Lett.*, 8(2020), No. 8, p. 283.
- [54] L.F. Liu, Q.Q. Ding, Y. Zhong, J. Zou, J. Wu, Y.L. Chiu, J.X. Li, Z. Zhang, Q. Yu, and Z.J. Shen, Dislocation network in additive manufactured steel breaks strength-ductility trade-off, *Mater. Today*, 21(2018), No. 4, p. 354.
- [55] Z. Li, B. He, and Q. Guo, Strengthening and hardening mechanisms of additively manufactured stainless steels: The role of cell sizes, *Scripta Mater.*, 177(2020), p. 17.
- [56] Y. Chew, G.J. Bi, Z.G. Zhu, F.L. Ng, F. Weng, S.B. Liu, S.M.L. Nai, and B.Y. Lee, Microstructure and enhanced strength of laser aided additive manufactured CoCrFeNiMn high entropy alloy, *Mater. Sci. Eng. A*, 744(2019), p. 137.
- [57] Z. Wang, Y.D. Huang, A. Srinivasan, Z. Liu, F. Beckmann, K.U. Kainer, and N. Hort, Hot tearing susceptibility of binary Mg-Y alloy castings, *Mater. Des.*, 47(2013), p. 90.
- [58] M.A. Easton, M.A. Gibson, S. Zhu, and T.B. Abbott, An a priori hot-tearing indicator applied to die-cast magnesium–rare earth alloys, *Metall. Mater. Trans. A*, 45(2014), No. 8, p. 3586.
- [59] Z.Q. Wei, Y. Wang, and Z. Liu, Effects of Zn and Y on hot-tearing susceptibility of Mg-xZn-2xY alloys, *Mater. Sci. Technol.*, 34(2018), No. 16, p. 2001.
- [60] D. Tomus, Y. Tian, P.A. Rometsch, M. Heilmaier, and X.H. Wu, Influence of post heat treatments on anisotropy of mechanical behaviour and microstructure of Hastelloy-X parts produced by selective laser melting, *Mater. Sci. Eng. A*, 667(2016), p. 42.
- [61] D.C. Kong, C.F. Dong, X.Q. Ni, L. Zhang, C. Man, and X.G. Li, Hetero-deformation induced stress in additively manufactured 316L stainless steel, *Mater. Res. Lett.*, 8(2020), No. 10, p. 390.
- [62] D.C. Kong, X.Q. Ni, C.F. Dong, L. Zhang, C. Man, X.Q. Cheng, and X.G. Li, Anisotropy in the microstructure and mechanical property for the bulk and porous 316L stainless steel fabricated via selective laser melting, *Mater. Lett.*, 235(2019), p. 1.
- [63] Q.Q. Han, Y.C. Gu, S. Soe, F. Lacan, and R. Setchi, Effect of hot cracking on the mechanical properties of Hastelloy X superalloy fabricated by laser powder bed fusion additive manufacturing, *Opt. Laser Technol.*, 124(2020), art. No. 105984.
- [64] X.Y. Wang, K. Kurosawa, M. Huang, X.K. Lu, D. Zhang, H. Kokawa, Y.B. Yan, and S. Yang, Control of precipitation behaviour of Hastelloy-X through grain boundary engineering, *Mater. Sci. Technol.*, 33(2017), No. 17, p. 2078.